Could a Pile of Slippery Sacks Behave Like an Ocean?

Patrick T. Haertel and David A. Randall

Department of Atmospheric Science, Colorado State University, Fort Collins, Colorado

ABSTRACT

A method for simulating fluid motions that shows promise for application to the oceans is explored. Incompressible inviscid fluids with free surfaces are represented as piles of slippery sacks. A system of ordinary differential equations governs the motions of the sacks, and this system is solved numerically in order to simulate a nonlinear deformation, internal and external gravity waves, and Rossby waves. The simulations are compared to analytic and finite-difference solutions, and the former converge to the latter as the sizes of the sacks are decreased.

The slippery-sack method appears to be well suited to ocean modeling for the following reasons: 1) it perfectly conserves a fluid's distributions of density and tracers; 2) unlike existing isopycnic models the slippery-sack method is capable of representing a continuum of fluid densities and vertically resolving neutral regions; 3) the inclusion of continuous topography adds no numerical complexity to the slippery-sack method; 4) the slippery-sack method conserves energy in the limit as the time step approaches zero; and 5) the slippery-sack method is computationally efficient.

1. Introduction

Consider a pile of sacks. We are not concerned with what the sacks contain, but if it helps, the reader may imagine them to contain sand or fluid. Suppose that there are no vertical gaps between sacks and that the sacks are slippery (Fig. 1). One would expect such a pile to be dynamic. For example, one might expect the pile depicted in Fig. 1 to spread with time. It turns out that under certain conditions a pile of slippery sacks behaves very much like a pool of fluid with the same mass distribution. Predicting the motions of a number of sacks is in general much easier than solving the partial differential equations that describe fluid motion in an Eulerian framework, so it would seem that treating a fluid as a collection of slippery sacks might be a viable alternative to traditional methods of simulating free-surface fluid motions, in particular, ocean circulations. In this paper we explore this idea. We begin by reviewing existing numerical methods for ocean models, noting where there is room for improvement.

a. Major classes of ocean models

At the present time there are three main classes of ocean models that are distinguished by the vertical coordinates they use to solve the equations of motion.

Most of the models within these classes use latitude and longitude as horizontal coordinates.

1) z-coordinate models

The majority of ocean models use depth or z as a vertical coordinate. Most such models are based on the method presented by Bryan (1969) but include modifications such as a free upper surface (Dukowicz and Smith 1994) or alternative advection schemes. While z-coordinate models have simulated ever more realistic circulations as advances in supercomputing have allowed ever higher resolutions (Smith et al. 2000), they have a few persistent problems. Deep water originates in a handful of locations and then is transported great distances nearly "adiabatically," with little modification to salinity or potential temperature. While mixing does modify temperature and salinity slightly in nature, z-coordinate models produce too much such mixing across isopycnic surfaces owing to numerical effects (Griffies et al. 2000). In some cases this spurious diapycnal mixing results in distorted deep water circulations (Roberts et al. 1996). While numerical techniques, such as isoneutral diffusion (Griffies et al. 1998), have been developed to minimize spurious diapycnal mixing, the problem has not been fully solved, and incorporating the new techniques increases model complexity. A second weakness of z-coordinate models is that many have step topography and poorly resolve the ocean bottom. Using shaved-cell (Adcroft et al. 1997) or partial-cell

Corresponding author address: Dr. Patrick T. Haertel, Dept. of Atmospheric Science, Colorado State University, Fort Collins, CO 80523-1371.
E-mail: haertel@atmos.colostate.edu
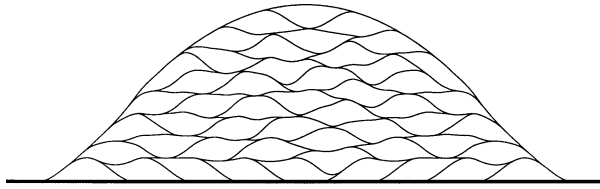
FIG. 1. A pile of slippery sacks having no gaps in the vertical.

topography (Pacanowski and Gnanadesikan 1998) alleviates this problem but also adds to model complexity.

2) ISOPYCNIC MODELS

Within a second category of ocean models, isopycnic models, the ocean is treated as a stack of layers, each having a constant potential density (Bleck 1998). Such models avoid spurious diapycnal mixing and have continuous topography, but they poorly resolve flow in weakly stratified regions and represent only a discrete set of potential densities. Moreover, isopycnic models effectively treat seawater as incompressible and, therefore, are unable to simulate horizontal pressure gradients associated with variations in compressibility that presumably contribute to the observed thermohaline circulation in the Atlantic (Sun et al. 1999).

3) σ-COORDINATE MODELS

The third major category consists of terrain-following or σ-coordinate models (Ezer and Mellor 1997; Haidvogel et al. 2000). This vertical coordinate was originally designed for simulating atmospheric circulations (Phillips 1957). While oceanic σ-coordinate models represent continuous topography, they suffer from a problem that has plagued atmospheric σ-coordinate models for years; near regions of steep topography two terms with nearly equal magnitude and opposite sign nearly cancel yielding errors in the calculation of the pressure gradient (Haney 1991). Like z-coordinate models, σ-coordinate models are also prone to spurious diapycnal mixing.

b. Alternative methods for ocean modeling

While most, if not all, full-fledged ocean models fit into one of the three classes discussed above, a number of other numerical techniques have been used for more idealized ocean simulations or are in the development stage for use in ocean models. Two examples are the particle-in-cell (PIC) method and finite-element methods (e.g., Lynch et al. 1995; Le Roux et al. 2000). Because the PIC method has much in common with the slippery-sack method, we review it in detail.

THE PIC METHOD

Developed at Los Alamos in 1955, the PIC method was originally intended for simulating fluid circulations involving large distortions, large slips, or colliding interfaces (Harlow 1964). Under the method the fluid's domain is divided into cells that are fixed in space, and the fluid's mass is distributed among a number of particles whose positions and velocities are prognosed. The amount of mass in each cell is calculated by summing the contributions from the particles in that cell (and from particles in nearby cells, in some implementations), and the mass field is then used to calculate a pressure field. A finite-difference approximation of the pressure gradient is used to determine particle accelerations. The PIC approach is a quasi-Lagrangian method; it combines respective strengths of Lagrangian and Eulerian approaches, the accurate Lagrangian treatment of mass transport and the simple Eulerian calculation of the pressure gradient.

Oceanic applications of the PIC method have involved idealized one- and two-layer systems. Pavia and Cushman-Roisin (1988) adapted the PIC method to the two-dimensional shallow water equations under the frontal-geostrophic approximation in order to simulate the evolution of oceanic warm-core eddies. They later developed a version of the model without the frontal-geostrophic approximation and simulated the merging of two oceanic eddies (Pavia and Cushman-Roisin 1990). Pavia (1992), Pavia and Lopez (1994), and Sanson et al. (1998) performed similar simulations of evolving oceanic eddies and frontal filaments. Ochoa et al. (1998) generalized a PIC shallow water model so that it allowed variable particle densities, and Esenkov and Cushman-Roisin (1999) and Cushman-Roisin et al. (2000) discuss the application of the PIC approach to a single layer within a two-layer system.

c. Motivation for studying the slippery-sack method

As the reader will soon find out, the slippery-sack method has a number of properties that make it well suited for simulating ocean circulations. Most importantly, under the slippery-sack method the mixing of density and tracers only occurs when it is explicity parameterized. Therefore, the slippery-sack method avoids the spurious diapycnal mixing that occurs in z- and σ-coordinate models. Of course, existing isopycnic models also avoid this problem, but the slippery-sack method has capabilities above and beyond these models as well, including higher vertical resolution in neutral regions, the ability to represent a continuum of densities, and explicit control over isopycnal mixing. Other advantages of the slippery-sack method are that it represents continuous topography without numerical complexity, it conserves energy in the limit as the time step approaches zero, and it is computationally efficient.

This paper discusses the first stage in the development of a slippery-sack ocean model, the creation and testing of an inviscid incompressible free-surface fluid model based on the slippery-sack method. The paper is organized as follows. Section 2 describes the dynamics of

a pile of slippery sacks, section 3 details the slippery-sack model, section 4 compares slippery-sack simulations to analytic and finite-difference solutions, section 5 compares the slippery-sack method to other numerical methods for the oceans and outlines the steps needed to transform the slippery-sack incompressible-fluid model into an ocean model, and section 6 is a summary.

2. Slippery-sack dynamics

Given a few assumptions, a surprisingly simple system of equations governs the motions of slippery sacks within a pile. In this section we derive such a system and discuss a few of its properties.

a. Properties of slippery sacks

We assume that slippery sacks have the following properties: 1) the horizontal mass distribution of a sack is independent of time within the sack's frame of reference; 2) when sacks slide over one another they conform so there are no vertical gaps between sacks; 3) pressure is hydrostatic within a pile of sacks; 4) density is a non-increasing function of height within a pile of sacks (i.e., when two sacks of differing densities collide the sack with the higher density slides under the sack with a lower density); and 5) a sack is accelerated in the horizontal by the integrated pressure force acting on the surface of the sack. These properties are selected with the hope that a pile of sacks will behave like a hydrostatic fluid with a free surface. They also make for easy calculations of sack motions and guarantee stable stratification. To keep things simple in this paper we make three additional assumptions: 6) a sack's density is constant in space and time; 7) the horizontal boundaries of the domains of sacks are periodic; and 8) there is no friction between sacks. We plan to relinquish these assumptions under future applications of the slippery-sack method.

In order to illustrate our concept with a simple example we consider the motions of three slippery sacks (Fig. 2). Initially sacks 1 and 2 are motionless, and sack 3 is moving toward the right (Fig. 2a). Sack 3 has a lower density than sack 1, and as a result it rides up and over sack 1. Notice that while sack 3's horizontal mass distribution is time independent within the frame of reference moving with the sack, the shape of sack 3 changes with time (e.g., its right edge twists upward between Figs. 2a and 2b). Once sacks 1 and 3 overlap there is a nonzero pressure on the interface between the sacks, and the inward normal force resulting from pressure on the interface accelerates sack 3 toward the left and sack 1 toward the right (cf. velocity vectors between Figs. 2b and 2c). Eventually sacks 1 and 3 reach sack 2, which becomes wedged between them because it has an intermediate density (Fig. 2d).

Properties 1–8 make no mention of vertical motions or accelerations, but clearly sack 3 accelerates and
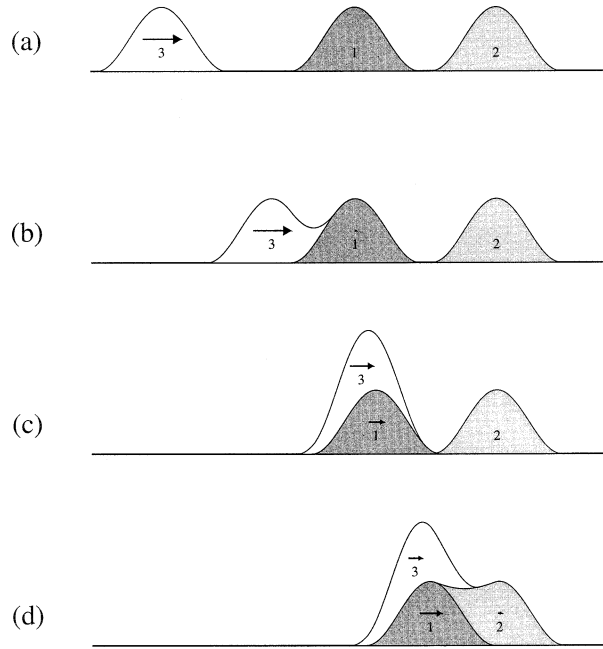
FIG. 2. (a)–(d) Three slippery sacks at four successive times; arrows indicate horizontal velocities; sack density increases with shading.

moves in the vertical as it rides up and over sacks 1 and 2 (Figs. 2a–d). In contrast with horizontal motions and accelerations, no single variable characterizes the vertical position or motion of the sack; different vertical cross sections of the sack have different vertical motions. For example, between Figs. 2a and 2b the right edge of sack 3 accelerates and moves upward but the remainder of the sack has zero vertical motion. As in the primitive equations, within a pile of slippery sacks the vertical motions and accelerations are driven by horizontal motions and accelerations and constrained by mass continuity.

b. Equations of motion

We now derive a system of equations of motion for a collection of slippery sacks. Toward that end, it is helpful to assign a stacking order to the sacks. We number the sacks 1, 2, . . . , k and assume that when two sacks overlap, the sack with a lower number lies beneath the sack with a higher number. In order for property 4 to be satisfied, this requires that density be a nonincreasing function of stacking number. As we note later in the paper, when two sacks have the same density, for the purposes of calculating horizontal sack motions it makes no difference which has a lower stacking number.

The net force on sack i resulting from pressure on its surface is as follows:

$$\mathbf{F}_i = \int_{S_i} p\mathbf{n} \, dA, \qquad (1)$$

where S_i is the surface of the sack, p is pressure, $\mathbf{n}$

denotes the inward normal vector, and A is the area measure. Using the hydrostatic assumption and a little geometry we obtain an expression for the horizontal component of this force:

$$\mathbf{F}_{h_i} = \sum_{j=i+1}^{k} \rho_j g \int_{D_h} T_j \boldsymbol{\nabla}_h T_i \, dA$$

$$- \sum_{j=1}^{i-1} \rho_i g \int_{D_h} T_i \boldsymbol{\nabla}_h T_j \, dA, \qquad (2)$$

where ρ is density, g is gravity, D_h is the entire horizontal domain, T denotes vertical thickness (of a particular sack), and $\boldsymbol{\nabla}_h$ is the horizontal gradient operator. Since density is uniform within each sack, a sack's vertical thickness at a particular location is proportional to its mass density per horizontal area. So we have

$$T_i(\mathbf{x}_h, t) = \frac{m_i(\mathbf{x}_h - \mathbf{x}_{h_i}(t))}{\rho_i}, \qquad (3)$$

where $\mathbf{x}_h$ is an arbitrary horizontal position, t is time, $\mathbf{x}_{h_i}(t)$ is the position of the center of sack i, and m_i is the horizontal mass distribution function for sack i, which is defined in sack-relative coordinates. Strictly speaking the net pressure force on a given sack depends on every other sack in the pile; that is, the sums on the right-hand side of (2) are over all the sacks with higher and lower stacking numbers. However, in practice the thickness functions are nonzero only in small regions around sack centers, and only those terms in the sums involving pairs of sacks that overlap need to be evaluated.

We apply Newton's second law in the horizontal to obtain equations of motion:

$$\frac{d\mathbf{v}_{h_i}}{dt} + f\hat{k} \times \mathbf{v}_{h_i} = \frac{\mathbf{F}_{h_i}}{M_i}, \qquad (4)$$

$$\frac{d\mathbf{x}_{h_i}}{dt} = \mathbf{v}_{h_i}, \qquad (5)$$

where v_h denotes horizontal velocity, the frame of reference is rotating at f rad s^{-1}, $\hat{k}$ is the unit vector in the vertical, and M_i denotes the mass of sack i. Equations (2)–(5) form a closed system.

c. Including bottom topography

Within the system (2)–(5), sacks with a lower stacking number than a given sack affect the acceleration of that sack in the same way as does bottom topography. Therefore, an irregular lower boundary can be included in the system by defining the lowest sack(s) to be motionless and to have the shape of the desired topography. In other words, including bottom topography adds no complexity to the system.

d. The stacking-order-exchange property

One interesting property of the system (2)–(5) is that if every sack within a layer within the pile has the same density, exchanging the stacking number of two sacks within that layer will have no effect on their horizontal motions. This is apparent from inspection of (2); the result of such an exchange of stacking numbers is the transfer of terms between the two sums on the right-hand side of (2). This property generalizes by induction to layers; if two layers of sacks have the same density, their relative vertical positioning may be changed without having any effect on the horizontal motions of sacks within the layers.

e. Conservation properties

The system (2)–(5) conserves mass by definition, and in appendix B we show that it conserves momentum and energy.

3. A slippery-sack incompressible fluid model

We have constructed a numerical model that predicts the motions of slippery sacks within a pile by approximating the equations of motion that were derived in the previous section. This section details that model discussing the discretization of the equations, the mass distribution functions for the sacks, and how the model is initialized.

a. Spatial discretization

The challenge of solving (2)–(5) is finding an efficient and accurate way to evaluate (2). For certain classes of thickness functions it is possible to evaluate the integrals in (2) analytically, but in addition to being mathematically cumbersome, that approach has the following disadvantage. The number of operations required to calculate the accelerations of all of the sacks is proportional to the number of sacks times the average number of sacks in the vertical. This means that if the vertical resolution of the model is doubled, the number of operations per time step is quadrupled. This becomes incapacitating for three-dimensional simulations in which the pile is at least tens of sacks deep.

We discretize a version of (2) using a technique whose number of operations per time step is proportional to the number of sacks. To illustrate this technique we first use (A1)–(A2) to rewrite (2):

$$\mathbf{F}_{h_i} = \int_{D_h} \left\{ \boldsymbol{\nabla}_h T_i \left[\sum_{j=i+1}^{k} \rho_j g T_j \right] + \rho_i g \boldsymbol{\nabla}_h T_i \left[\sum_{j=1}^{i} T_j \right] \right\} dA. \quad (6)$$

We now approximate the integral in (6) using a generalized Riemann sum. Let R be a partition of D_h and for each $r \in R$ let $\mathbf{x}_r \in r$. For the simulations presented here R is a collection of identical rectangles, whose

widths in each dimension are one-fifth to one-tenth that of the smallest sack. The point x_r is considered to be a representative of r and for our purposes is selected to be at the center of r. The following equation approximates (6):

$$\mathbf{F}_{h_i} \approx \sum_{r \in R} \left\{ \mathbf{\nabla}_h T_i(\mathbf{x}_r, t) \left[\sum_{j=i+1}^{k} \rho_j g T_j(\mathbf{x}_r, t) \right] \right.$$

$$\left. + \; \rho_i g \mathbf{\nabla}_h T_i(\mathbf{x}_r, t) \left[\sum_{j=1}^{i} T_j(\mathbf{x}_r, t) \right] \right\} A(r), \quad (7)$$

where the gradients are evaluated analytically. Now for a given $r \in R$, each of the two sums within brackets differs by one term between i and $i + 1$, so the process of evaluating the sums for every sack overlapping x_r scales linearly with the number of sacks in the vertical. Moreover, the number of partition elements scales linearly with the number sacks in a given horizontal layer, so the process of evaluating (7) for every sack and for every $r \in R$ scales linearly with the total number of sacks.

Another advantage of using (7) to calculate sack accelerations is that the sum of the exact kinetic energy and the approximate potential energy, $\Sigma_{r \in R} \{ \int_{D_z} \rho(\mathbf{x}_r, z, t) gz \, dz \} A(r)$, is conserved in the limit as the time step approaches zero. In fact, the reason we rewrite (2) as (6) before discretizing is to achieve this conservation. When using (7) to calculate sack accelerations momentum is not in general conserved under continuous time, other than in the limit as $A(r)$ goes to zero. When (2) is discretized in the same manner rather than (6), momentum is conserved under continuous time but energy is not. We have been unable to find a discretization of (2)–(5) that conserves both energy and momentum (although such a discretization may well exist), and we elect to enforce the conservation of energy because that places a stronger constraint on the stability of the system than enforcing the conservation of momentum.

In order to implement (7) efficiently, one must keep track of the sacks that have the potential to overlap a given partition representative x_r. To do this we divide the horizontal model domain into rectangular subdomains that are half as wide as the largest sack in each horizontal dimension. Let s denote the subdomain containing x_r. Then, only those sacks centered in the eight subdomains surrounding s have the potential to have centers within a sack half-width of x_r in both the x and y directions, which means that only those sacks need to be included in the evaluation of the quantity in braces in (7).

b. Time discretization

The time derivatives in (4)–(5) are evaluated using second-order Adams–Bashforth time differencing. While such time differencing is weakly unstable for wave oscillations, for the simulations presented here the time steps and durations are sufficiently small (0.1– 0.001 and 2–5 s, respectively) that the errors associated with time differencing are much smaller than those associated with treating the fluid as a collection of sacks. In the future we plan to use third-order Adams–Bashforth time differencing, which is conditionally stable for wave oscillations, to facilitate long-duration simulations.

c. The mass distribution functions

The model uses mass distribution functions with the following form:

$$m_i(x, y) = \frac{4M_i}{w_{x_i} w_{y_i}} \left[\cos \left(\frac{\pi x}{w_{x_i}} \right) \right]^2 \left[\cos \left(\frac{\pi y}{w_{y_i}} \right) \right]^2 \quad (8)$$

for $|x| \leq w_{x_i}/2$ and $|y| \leq w_{y_i}/2$ (m_i is zero elsewhere), where x and y denote the horizontal displacement from the center of the sack, and w_{x_i} and w_{y_i} are the widths of the sack in the x and y directions, respectively. We chose this form for the mass distribution functions because it has several nice properties; it is continuous, it has a continuous horizontal gradient that vanishes at the edges of the sack, and it is easy to construct piles that are perfectly level using sacks with such a mass distribution. For two-dimensional simulations the y dependence of the mass distribution function is neglected, that is, it has the following form:

$$m_i(x) = \frac{2M_i}{w_{x_i}} \left[\cos \left(\frac{\pi x}{w_{x_i}} \right) \right]^2, \quad (9)$$

where M_i denotes the mass per unit span of sack i.

d. Initialization

There are many ways to select initial sack positions and mass distribution parameters so that a pile of sacks has approximately the same mass distribution as a pool of fluid. We use an initialization procedure that is well suited to fluids comprising layers of constant density. To illustrate the approach we discuss its use in the first simulation presented here, for which the fluid is a two-dimensional ridge having the shape of an inverted parabola (Fig. 3a). The basic idea is to divide the domain into divisions having equal width (Fig. 3b), to put the mass in each division into a single sack (Fig. 3c), and to stack the sacks so that there are no gaps in the vertical (e.g., Fig. 3d). The mathematical details of the procedure follow.

Let $\Delta x = 0.2$ denote the width of a domain division and suppose that $x = 0$ is the center of the ridge. The ridge is initially motionless, and its height is given by $h(x) = 1 - x^2$ for $-1 \leq x \leq 1$, $h(x) = 0$ for $|x| > 1$. Each sack's mass per unit span is defined to be the mass per unit span in the domain division it represents:
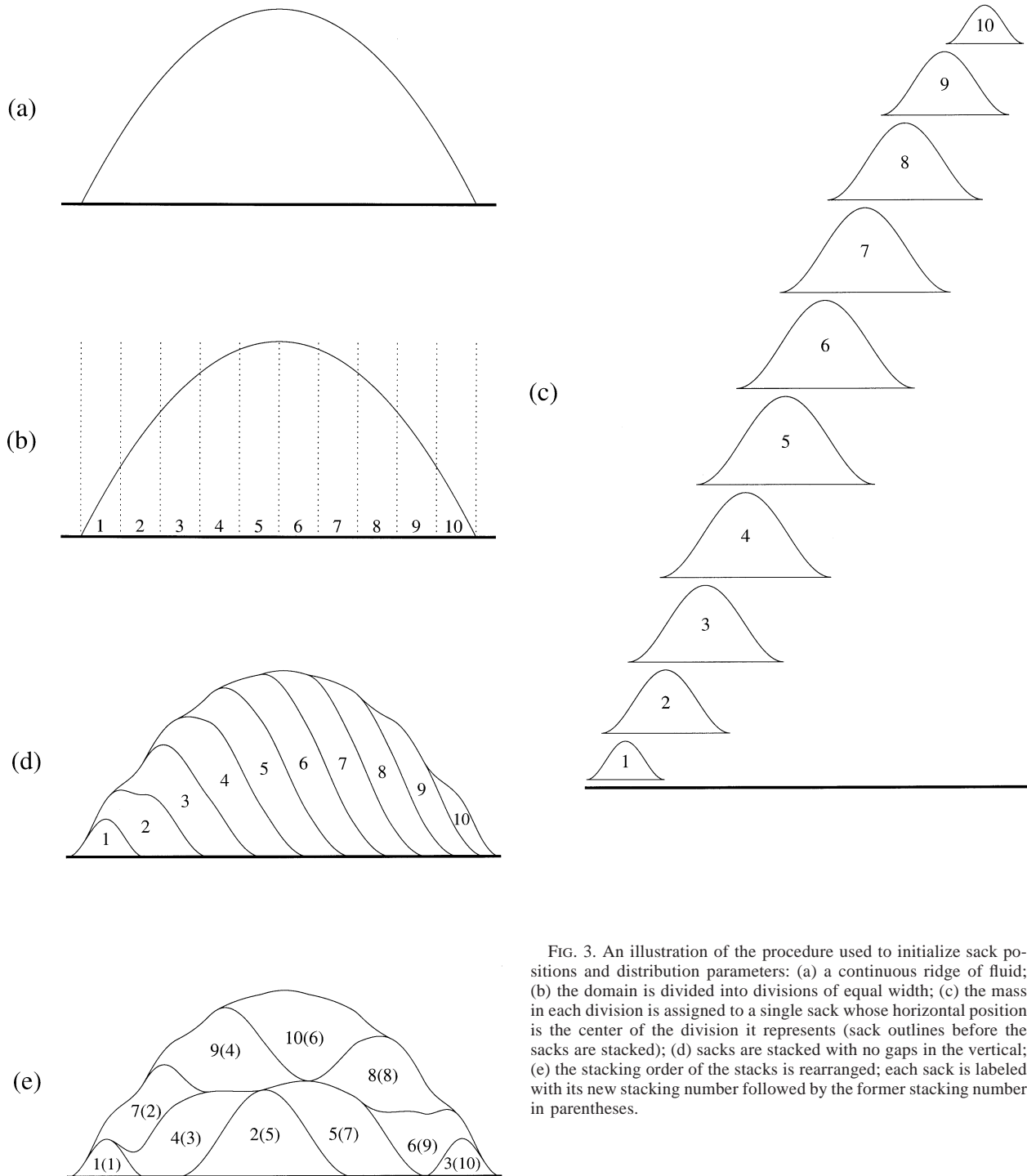
Fig. 3. An illustration of the procedure used to initialize sack positions and distribution parameters: (a) a continuous ridge of fluid; (b) the domain is divided into divisions of equal width; (c) the mass in each division is assigned to a single sack whose horizontal position is the center of the division it represents (sack outlines before the sacks are stacked); (d) sacks are stacked with no gaps in the vertical; (e) the stacking order of the stacks is rearranged; each sack is labeled with its new stacking number followed by the former stacking number in parentheses.

$$M_i = \int_{(i-1)\Delta x - 1}^{i\Delta x - 1} h\rho \, dx, \qquad (10)$$

where ρ is the density of the ridge and of each sack. Each sack's horizontal position is defined to be the center of the domain division that it represents:

$$x_i = \left(i - \frac{1}{2}\right)\Delta x - 1. \qquad (11)$$

The sack width is a free parameter, and we arbitrarily select it so that a sack's maximum vertical thickness is one-half of its width:

$$w_{x_i} = 2\sqrt{\frac{M_i}{\rho}}. \qquad (12)$$

The parameters M_i and w_{x_i} together with (9) define the mass distribution m_i, which is substituted into (3) to find the vertical thickness function T_i. When the sacks are stacked so that there are no gaps in the vertical, the height h_i of the upper surface of a sack is the sum of its vertical thickness and the vertical thicknesses of the sacks beneath it:

$$h_i(x, t) = \sum_{j=1}^{i} T_j(x, t). \qquad (13)$$

To obtain the pictures of sack outlines (e.g., Fig. 3d) we simply plot h_i for each sack. Since each sack has the same density, it makes no difference what stacking order we assign to the sacks; the mass distribution of the pile and the horizontal motions of the sacks are independent of stacking order (section 2d). For a more aesthetically pleasing pile, we select a new stacking order that minimizes the vertical extent of each sack (Fig. 3e).

The above illustration pertains to a two-dimensional fluid with a constant density. When the fluid has three dimensions, the domain is divided in both the x and y directions, that is, into grid boxes, and the fluid within each box is assigned to a single sack. When the fluid comprises multiple layers of constant density the above procedure is applied to each layer in succession.

4. Simulations

In this section we use the slippery-sack model described in the previous section to simulate three kinds of fluid motion: a nonlinear deformation, gravity waves, and Rossby waves. These three types of circulations were selected as test cases because each is inviscid and each occurs in the oceans.

a. The spreading ridge

Consider a ridge of fluid with the shape of an inverted parabola, a maximum depth of 1 m, a width of 2 m, and a density of 1000 kg m^{-3} on a nonrotating planet where the acceleration due to gravity is 1 m s^{-2}. If the ridge is initially at rest, there is no friction or viscosity, and nonhydrostatic pressure is neglected, then the motions of the ridge are described by an analytic solution (Frei 1993; Schär and Smolarkawicz 1996). We now check how accurately the slippery-sack model reproduces that solution. We represent the fluid using only 40 sacks (Fig. 4a). Sack mass distributions and positions are initialized according to the method described in section 3d.

Within the analytic solution the ridge maintains the shape of an inverted parabola as it spreads over time (Figs. 4a–c). The pile of sacks closely approximates that

shape; the top of pile, albeit wavy, is nearly collocated with the smooth top of the continuous ridge at 2 s (Fig. 4c). The analytic velocity field is a linear function of x, and for the most part the sack velocities lie on that line (Figs. 4d–f) with the only perceptible differences occurring at the outer edges of the ridge at 2 s (Fig. 4f).

The total energy of the pile is very nearly conserved with time (Fig. 4g); deviations from the initial value are about one-hundredth of one percent. To confirm that the model conserves energy in the limit as the time step approaches zero, we repeated the simulation multiple times successively halving the time step, and the deviation of the total energy from its initial value does indeed approach that expected from round-off errors.

We also repeated the simulation using both fewer and more sacks calculating the normalized velocity error, defined as the 11 norm of the difference between the slippery-sack and analytic velocity fields divided by the 11 norm of the analytic velocity field, for each simulation at 2 s (Fig. 4h). From these tests we draw two conclusions. First, for this test case the slippery-sack method is well-behaved at low resolution. Even when only 20 sacks are used the velocity field at 2 s is approximated within about 20%. Second, as the number of (size of the) sacks is increased (decreased) the behavior of the pile approaches that of the continuous ridge. We leave a discussion of the rate of convergence of the method to the following section; within the simulation presented there the sacks have identical mass distributions, and errors are related to sack size.

b. Internal and external gravity waves

Now consider a two-dimensional pool of fluid comprising two layers, the lower layer having a density of 1100 kg m^{-3} and the upper layer having a density of 1000 kg m^{-3}. The depth of each layer is 1 m, and the pool is 20 m wide with periodic boundaries. Suppose that we introduce into the lower layer a horizontal velocity perturbation having a magnitude of 1 mm s^{-1} and a Gaussian distribution in the horizontal with a width of 2 m. Such a perturbation projects onto both internal and external gravity waves, and we now test how well the slippery-sack method simulates these waves. The difference in density between the layers is much greater than that which occurs in the oceans; we select this stratification so that the phase speeds of the internal and external waves are not drastically different and the behavior of both may be studied within the same simulation. Since the initial velocity perturbation is very weak, its evolution is almost exclusively linear, and we compare a slippery-sack simulation to output from a linear Eulerian finite-difference model that uses centered fourth-order spatial differencing and leapfrog time differencing and is run at sufficiently high resolution that its output is treated as the continuous linear solution.

We represent each layer using 40 sacks that each have a width of 1 m (Fig. 5a). Because of our choice for a
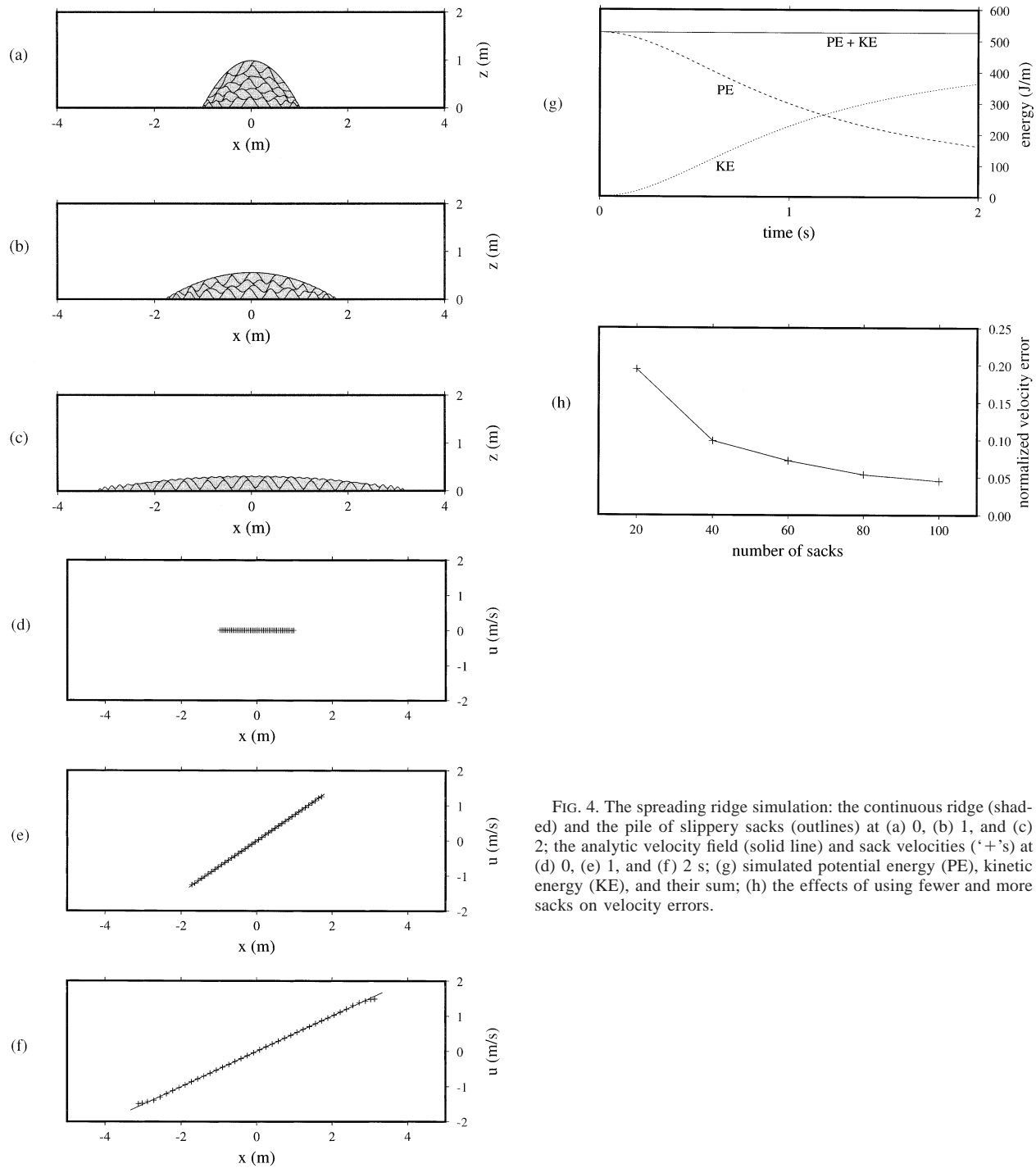
FIG. 4. The spreading ridge simulation: the continuous ridge (shaded) and the pile of slippery sacks (outlines) at (a) 0, (b) 1, and (c) 2; the analytic velocity field (solid line) and sack velocities ('+'s) at (d) 0, (e) 1, and (f) 2 s; (g) simulated potential energy (PE), kinetic energy (KE), and their sum; (h) the effects of using fewer and more sacks on velocity errors.

mass distribution function (8), the top of each layer is perfectly level. Each sack in the lower layer is initialized to have a velocity equal to the value of the Gaussian distribution at the location of its center, and sacks in the upper layer are initially motionless. The initial vertically averaged horizontal velocity in the lower layer of the pile is close to that in the continuous pool (Fig. 5b); the only significant errors in initialization occur

near the center of the perturbation and reach about 5% of the perturbation's magnitude.

Within both the slippery-sack and linear simulations the initial velocity perturbation in the lower layer divides into four humps (Figs. 5b–d). The outer two humps are the circulations of external gravity waves, and the inner two are associated with internal gravity waves (Fig. 5d). Although the upper layer is initially
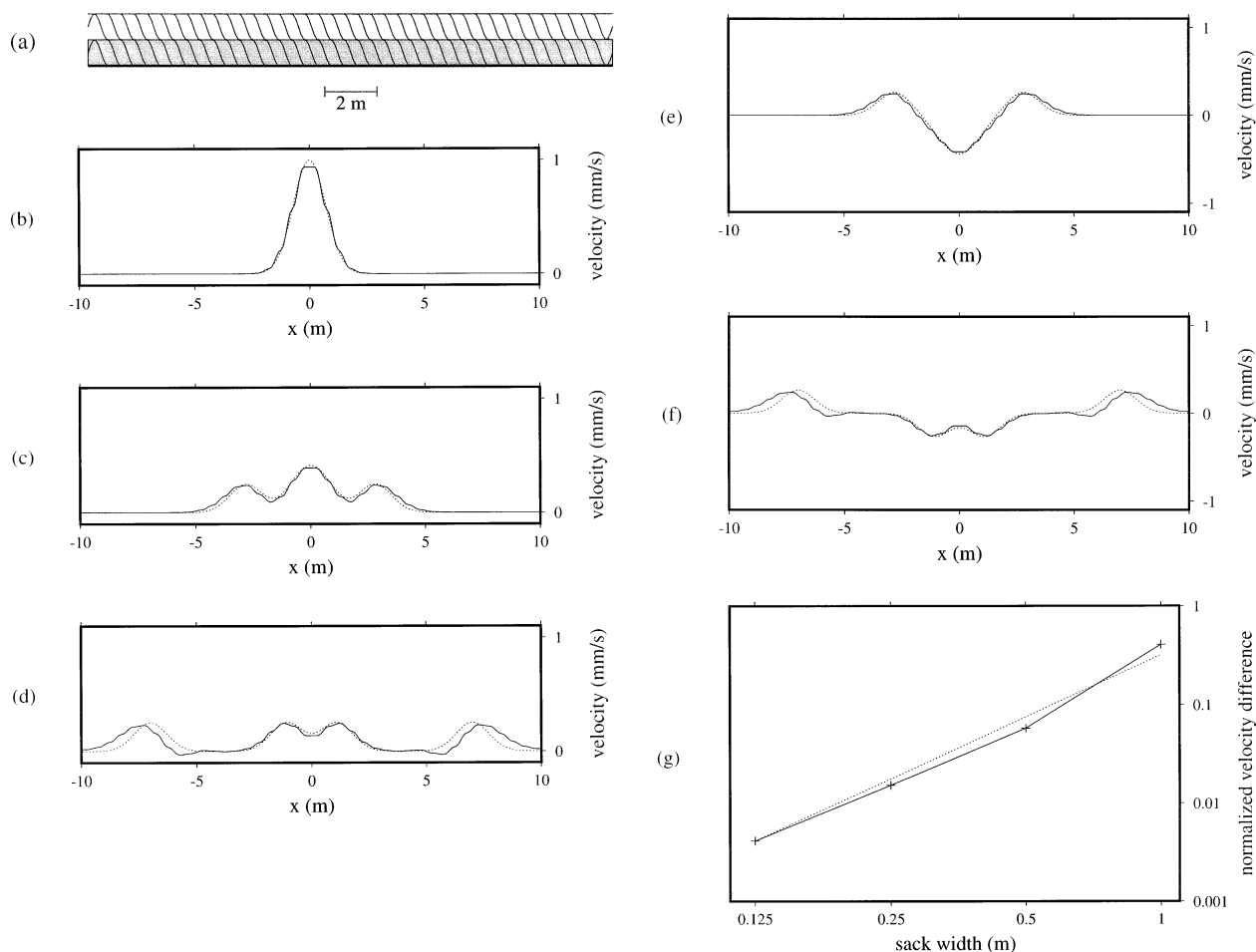
FIG. 5. The gravity wave simulation. (a) The initial state of the pile of sacks. Sacks within the lower layer (shaded) are 10% more dense than those within the upper layer. Vertically averaged velocity within the lower layer of the pile of slippery sacks (solid line) and the continuous fluid (dotted line) at (b) 0, (c) 2, and (d) 5 s; vertically averaged velocity within the upper layer of the pile of slippery sacks (solid line) and the continuous fluid (dotted line) at (e) 2 and (f) 5 s; (g) the normalized difference between the slippery-sack and linear lower-layer velocity fields at 5 s for several sack sizes. The dotted line has a slope of -2.

undisturbed (not shown), at later times the waves are apparent in this layer as well (Figs. 5e–f). The slippery-sack waves propagate too quickly and show evidence of dispersion (Figs. 5d,f), but considering that the width of each sack is only one-half that of the initial momentum perturbation, the waves are surprisingly well represented.

To measure the rate of convergence of the slippery-sack simulation to the linear solution we repeatedly reduce the sack size by a factor of 2 in each dimension and compare the logarithm of the normalized velocity difference to the logarithm of sack width (Fig. 5g). The points lie close to a line with a slope of -2, which means that the normalized velocity difference is approximately proportional to the square of the sack width. Both errors associated with the slippery-sack method and nonlinear effects contribute to this velocity difference, but for the purpose of creating this plot we reduced the amplitude of the initial perturbation to 10^{-6} mm s^{-1}

so that based on scaling arguments we would expect the latter to be orders of magnitude smaller than the former. Therefore, the normalized velocity difference may be thought of as the approximate normalized velocity error for the simulations depicted in Fig. 5g, and we conclude that this error is approximately proportional to the square of the sack width.

c. Rossby waves

For a final test case we consider a three-dimensional pool of fluid with a constant density of 1000 kg m^{-3} that is 1 m deep and 10 m across in each horizontal direction. Suppose that the Coriolis force $f = \beta y$, where $\beta = 1$ s^{-1} m^{-1}, and that initially there is a cyclonic vortex located at the center of the pool with a scale of about 2-m and a maximum velocity of about 1 mm s^{-1} (Fig. 6a). Such a vortex projects largely onto Rossby and mixed Rossby–gravity waves, and we now see how
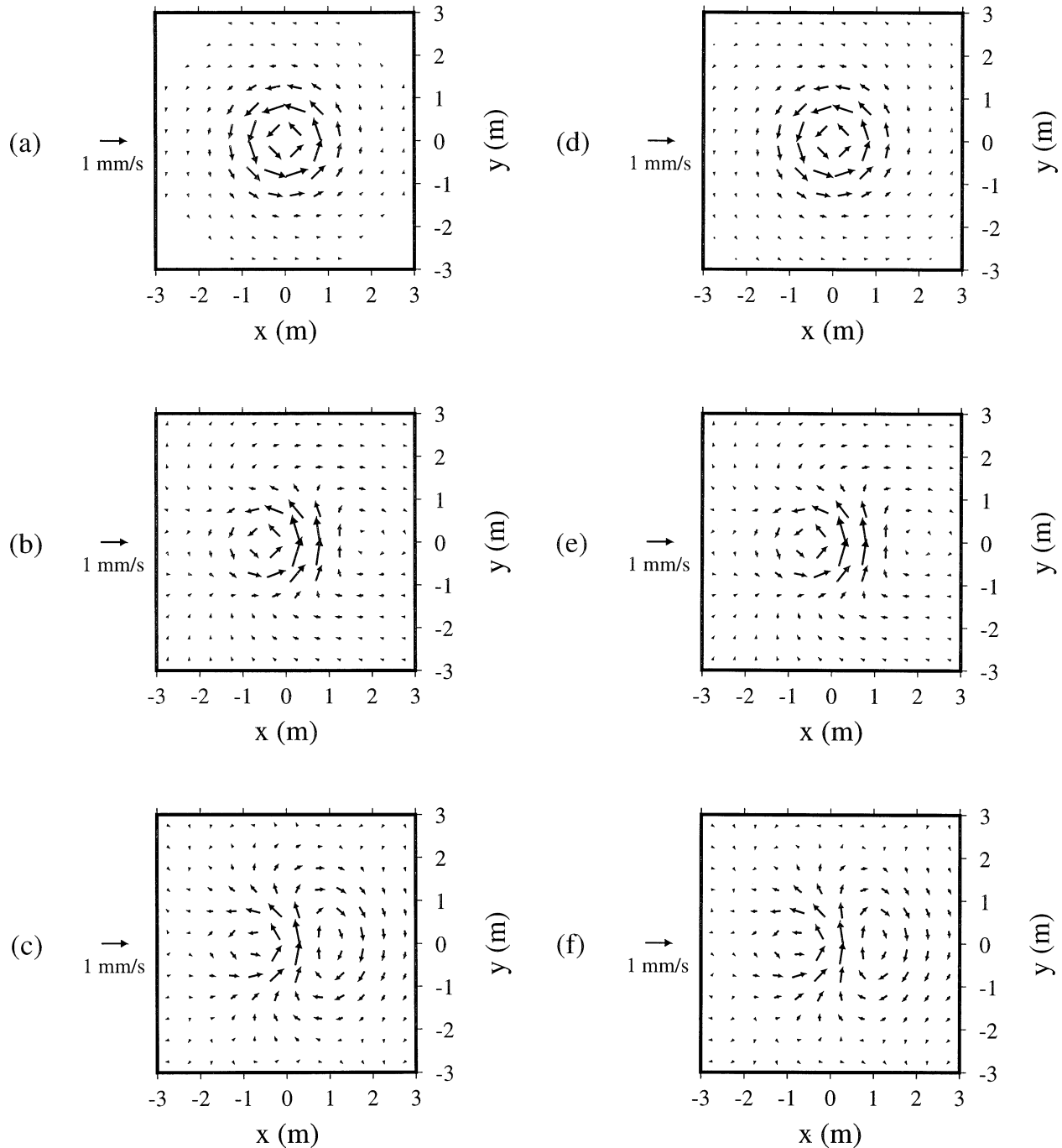
FIG. 6. The Rossby wave simulation: The finite-difference velocity field at (a) 0, (b) 1.5, and (c) 3 s; the slippery-sack velocity field at (d) 0, (e) 1.5, and (f) 3 s.

well the slippery-sack method simulates its evolution. Once again we use a finite-difference model to obtain the linear solution for comparison. For both the slippery-sack and finite-difference simulations the horizontal boundaries are periodic, but the duration of the simulations is sufficiently short that the flow at the boundaries remains undisturbed. We use 1600 sacks, each hav-

ing a width of 1 m in each horizontal dimension, to represent the pool. The sack centers are initially positioned in a 40 × 40 matrix of points having a separation distance of 0.25 m, again making for a perfectly level surface.

Within both the pool and the pile the vortex migrates in the negative x direction and weakens, and an anti-

cyclonic circulations develops to its right (Figs. 6a–f). At 3 s the circulations within the slippery-sack simulation are slightly too weak (Fig. 6f) with the average magnitude of the difference between the linear and slippery-sack velocity fields being 0.015 mm s^{-1}. As in the previous simulations, when the sack sizes are reduced the slippery-sack solution rapidly converges to the linear solution (not shown).

5. Discussion

We have shown that the slippery-sack method is capable of simulating several kinds of circulations that occur in incompressible fluids, and that it has several properties that would seem to make it well suited for simulating ocean circulations. In this section we compare the slippery-sack method to related numerical methods and to mainstream ocean methods and discuss plans for transforming the slippery-sack model described in section 3 into an ocean model.

a. A summary of the slippery-sack method

Under the slippery-sack method a fluid is represented as a pile slippery sacks with no vertical gaps between sacks. Neutral or stable stratification is built into the method; each sack is constrained to lie above other sacks having greater density. Each sack is accelerated in the horizontal according to the integrated normal force resulting from pressure on its surface. The integration is approximated using a generalized Riemann sum in such a way that the total energy of the system is conserved in the limit as the time step approaches zero, and the number of operations per time step is proportional to the number of sacks. The method has been successfully used to simulate several kinds of inviscid incompressible fluid circulations, including a nonlinear deformation, gravity waves, and Rossby waves.

b. Slippery-sack versus oceanic applications of the PIC method

Although conceived from quite different philosophies, our implementation of the slippery-sack method and previous oceanic applications of the PIC method are quite similar (for a review of the latter see section 1b). Under both methods mass is carried by parcels (sacks/particles) whose horizontal positions and velocities are prognosed. Moreover, prior to calculating parcel accelerations both methods calculate pressure or thicknesses and their gradients on a set of points fixed in space. However, the two approaches have differences relating to 1) the treatment of vertically varying flows and 2) the horizontal acceleration of parcels.

Under the slippery-sack approach sacks are conceived as having a vertical extent and a stacking order. This allows for the diagnosing of sack heights and the simulation of vertically varying flows without separate treatment of fluid layers. In contrast, in previous oceanic applications of the PIC method, the vertical positions of particles are not monitored except, in some cases, for their association with a particular layer. The PIC method may of course be applied with cell divisions in the vertical as well as the horizontal, but the authors are unaware of any such applications to the ocean.

A second distinction between the slippery-sack method and previous oceanic applications of the PIC method is that, under the latter, particles are accelerated by calculating the pressure gradient on a grid and interpolating it to particle positions, whereas under the former, the normal component of the pressure force is averaged over the surface of the sack for the purpose of accelerating sacks.

c. Slippery-sack versus SPH

Smooth Particle Hydrodynamics (SPH), a Lagrangian method that has been applied to a variety of fluid dynamical problems including free surface flows (Monaghan 1992), is also related to the slippery-sack method. Each method prognoses the positions and velocities of a number of fluid parcels (points/sacks) and calculates spatial gradients through analytic differentiation of basis functions (interpolating kernal/mass distribution functions). The methods again differ according to their treatment of the vertical dimension. Within SPH the vertical positions of points are prognosed, requiring the introduction of artificial compressibility for fluids having free surfaces (Monaghan 1994). In contrast, under the slippery-sack method the vertical positions of sacks are implicitly diagnosed from their stacking order. Another difference between the two methods is that SPH is gridless, whereas under the slippery-sack method sack thicknesses and their gradients are evaluated on a set of points fixed in space.

d. Slippery-sack versus isopycnic methods

The slippery-sack method takes the philosophy behind the use of an isopycnic vertical coordinate but applies it in the horizontal as well as the vertical. In addition to avoiding advection errors in the horizontal, as is mentioned above, this facilitates the simulation of vertically dependent flows without partitioning the fluid into layers. Each sack can have a unique density (that will eventually be allowed to change continuously in time), so unlike existing isopycnic models, the slippery-sack method may represent a continuum of fluid densities. Another difference between the slippery-sack method and the isopycnic approach is that, under the former, vertical resolution depends on the choice of mass distribution functions and is time independent, whereas under the latter, vertical resolution depends on the vertical gradient of potential temperature and varies in both space in time. Thus, the slippery-sack method provides better vertical resolution in neutral regions, but

the isopynic approach provides better vertical resolution in stable regions.

e. *Slippery-sack versus z- and σ-coordinate methods*

The slippery-sack method appears to have advantages over both z- and σ-coordinate methods related to both mixing and topography. Under the slippery-sack method, mass properties are exactly conserved and mixing occurs only if it is explicitly parameterized. The slippery-sack method also represents continuous topography with an analytic calculation of thickness gradients (i.e., no analog to σ-coordinate pressure-gradient errors) and without numerical complexity.

f. *A disadvantage/advantage of using time-independent mass distributions*

Under our implementation of the slippery-sack method, sacks have time-independent mass distributions. Therefore, if a layer is only several sacks deep and it diverges substantially in the horizontal, it eventually becomes a series of fluid lumps rather than a shallow continuous layer of fluid. The pile of sacks is just starting to do that at the end of the spreading ridge simulation (Fig. 4c), and eventually there are substantial errors in the height field as a result. However, in nature when a fluid layer diverges substantially it often pinches off (e.g., dewatering on a tidal flat), and having time-independent mass distributions allows the model to simulate this process in a natural way.

g. *Toward a slippery-sack ocean model*

The model described in section 3 represents a three-dimensional inviscid incompressible fluid with a free surface. We are in the process of transforming the model into an ocean model by adding the features listed below.

1) MIXING

Much of the circulation of the world's oceans is driven by wind stress forcing at the surface that is communicated to lower levels through the vertical mixing of momentum. Such mixing will be represented by allowing sacks that are in contact with one another to exchange momentum. This will also have the effect of diffusing momentum in the horizontal. The mixing of density and tracers will be treated in a similar way.

2) DIABATIC EFFECTS/COMPRESSIBILITY

The slippery-sack model will be modified to allow compressible sacks. A single value of potential temperature and salinity will be assigned to each sack and allowed to vary in time, and an average sack density will be diagnosed using an equation of state. This diagnosis requires the knowledge of a mean sack pressure,

which is determined by the weight of sacks above. Following the diagnosis of density the remainder of the time step will be the same as that for the incompressible model. Sacks will still have fixed horizontal mass distributions, so all of the compression will take place in the vertical. The hydrostatic approximation will be maintained, so there will be no vertically propagating sound waves.

3) LONG TIME STEPS

Under the slippery-sack method the pile has a free surface and supports the rapid oscillations of the external mode. In the interest of reducing run times most ocean models that support this mode either use time splitting or else implicit time differencing (Dukowicz and Smith 1994). We plan to slow the external mode using the gravity wave retardation method, which Jensen (1996, 2001) used to lengthen time steps by factors of 4–10.

6. Summary

In this paper it is shown that under certain conditions piles of slippery sacks behave like pools of fluid. A slippery-sack numerical model is used to simulate a nonlinear deformation, internal and external gravity waves, and Rossby waves in incompressible fluids with free surfaces. The simulations converge to analytic and high-resolution finite-difference solutions as the sizes of the sacks are decreased.

The slippery-sack method appears to be well suited to ocean modeling. It is computationally efficient, has favorable conservation properties, and it circumvents several problems that occur in existing ocean models. In particular, the slippery-sack method avoids spurious diapycnal mixing, and in contrast to existing isopycnic models it can represent a continuum of densities and can resolve neutral regions in the vertical. The authors are in the process of transforming their slippery-sack model into an ocean model.

APPENDIX A

Identities Involving Thickness Functions

The following properties of the thickness functions are used throughout the paper:

$$\frac{\partial T_i}{\partial t} = -\mathbf{v}_{h_i} \cdot \boldsymbol{\nabla}_h T_i, \tag{A1}$$

$$\int_{D_h} T_i(\boldsymbol{\nabla}_h T_j) \, dA = -\int_{D_h} T_j(\boldsymbol{\nabla}_h T_i) \, dA, \tag{A2}$$

$$\int_{D_h} T_i(\boldsymbol{\nabla}_h T_i) \, dA = 0, \tag{A3}$$

where all variables are defined in section 2. To obtain (A1) we apply the chain rule to (3), and to obtain (A2), (A3), we make use of the periodic boundary condition (property 7, section 2a).

APPENDIX B

Conservation Properties

a. Conservation of momentum

Let $\mathbf{P}'$ denote the total horizontal momentum of a pile of k slippery sacks. Here the prime ($'$) notation denotes that the vector is represented in nonrotating coordinates. Then we have

$$\frac{d\mathbf{P}'}{dt} = \frac{d}{dt}\left(\sum_{i=1}^{k} M_i \mathbf{v}'_{h_i}\right) = \sum_{i=1}^{k} M_i\left(\frac{d\mathbf{v}_{h_i}}{dt} + f\hat{k} \times \mathbf{v}_{h_i}\right). \tag{B1}$$

Substituting into (B1) using (2), (4) yields

$$\frac{d\mathbf{P}'}{dt} = \sum_{i=1}^{k}\left[\sum_{j=i+1}^{k} \rho_j g \int_{D_h} T_j \boldsymbol{\nabla}_h T_i \, dA\right] - \sum_{i=1}^{k}\left[\sum_{j=1}^{i-1} \rho_i g \int_{D_h} T_i \boldsymbol{\nabla}_h T_j \, dA\right]. \tag{B2}$$

We rewrite the double sums in a manner that does not indicate the order of summation (because the sums have a finite number of terms; their order of summation is unimportant):

$$\frac{d\mathbf{P}'}{dt} = \sum_{j>i} \rho_j g \int_{D_h} T_j \boldsymbol{\nabla}_h T_i \, dA - \sum_{j<i} \rho_i g \int_{D_h} T_i \boldsymbol{\nabla}_h T_j \, dA, \tag{B3}$$

where within the sums on the right-hand side i and j range over the values between and including 1 and k that satisfy the given condition. Now swapping the index *names* does not alter a sum, and if this is done to either sum on the right-hand side of (B3), it is apparent that the two sums are identical, which means that the right-hand side is zero and that the total horizontal momentum is conserved.

b. Conservation of energy

Let KE denote the total kinetic energy (neglecting vertical motion) of the pile. Then we have

$$\frac{d}{dt}(\text{KE}) = \frac{d}{dt}\left(\sum_{i=1}^{k} \frac{1}{2} M_i |\mathbf{v}'_{h_i}|^2\right) = \frac{d}{dt}\left(\sum_{i=1}^{k} \frac{1}{2} M_i |\mathbf{v}_{h_i}|^2\right)$$

$$= \sum_{i=1}^{k} \mathbf{v}_{h_i} \cdot M_i \frac{d\mathbf{v}_{h_i}}{dt}. \tag{B4}$$

Substituting into (B4) using (2), (4) yields

$$\frac{d}{dt}(\text{KE}) = \sum_{i=1}^{k} \mathbf{v}_{h_i} \cdot \left[\sum_{j=i+1}^{k} \rho_j g \int_{D_h} T_j \boldsymbol{\nabla}_h T_i \, dA\right.$$

$$\left. - \sum_{j=1}^{i-1} \rho_i g \int_{D_h} T_i \boldsymbol{\nabla}_h T_j \, dA\right]. \tag{B5}$$

As before, we rewrite the double sums in a manner that does not indicate an order of summation:

$$\frac{d}{dt}(\text{KE}) = \sum_{j>i}\left(\rho_j g \mathbf{v}_{h_i} \cdot \int_{D_h} T_j \boldsymbol{\nabla}_h T_i \, dA\right)$$

$$- \sum_{j<i}\left(\rho_i g \mathbf{v}_{h_i} \cdot \int_{D_h} T_i \boldsymbol{\nabla}_h T_j \, dA\right). \tag{B6}$$

Now consider the time–rate of change of potential energy:

$$\frac{d}{dt}(\text{PE}) = \frac{d}{dt}\left(\int_D \rho g z \, dV\right)$$

$$= \frac{d}{dt}\int_{D_h}\left\{\sum_{i=1}^{k} \rho_i g \frac{(z_{t_i}^2 - z_{b_i}^2)}{2}\right\} dA, \tag{B7}$$

where D is the entire domain, $z_{t_i}(\mathbf{x}_h, t)$ denotes the height of the top of sack i, and $z_{b_i}(\mathbf{x}_h, t)$ denotes the height of the bottom of sack i. Substituting for the height variables and simplifying yields

$$\frac{d}{dt}(\text{PE}) = \frac{d}{dt}\int_{D_h}\left\{\sum_{i=1}^{k} \rho_i g\left[T_i\left(\sum_{j=1}^{i-1} T_j\right) + \frac{1}{2}T_i^2\right]\right\} dA. \tag{B8}$$

After applying Leibniz's rule and rewriting the double sums we have

$$\frac{d}{dt}(\text{PE}) = \sum_{j<i} \rho_i g \int_{D_h} T_i \frac{\partial T_j}{\partial t} \, dA + \sum_{j<i} \rho_i g \int_A T_j \frac{\partial T_i}{\partial t} \, dA$$

$$+ \sum_{i=1}^{k} \rho_i g \int_{D_h} T_i \frac{\partial T_i}{\partial t} \, dA. \tag{B9}$$

Using (A1) to substitute for the terms having time derivatives on the right-hand side of (B9), swapping the index names within the first sum, applying (A2) to the second sum, and applying (A3) to the third sum making it vanish yields

$$\frac{d}{dt}(\text{PE}) = -\sum_{j>i} \left(\rho_j g \mathbf{v}_{h_i} \cdot \int_{D_h} T_j \boldsymbol{\nabla}_h T_i \, dA \right)$$

$$+ \sum_{j<i} \left(\rho_i g \mathbf{v}_{h_i} \cdot \int_{D_h} T_i \boldsymbol{\nabla}_h T_j \, dA \right). \quad (\text{B10})$$

Now the right-hand side of (B10) equals the negative of the right-hand side of (B6), so the sum of the time–rates of change of the kinetic and potential energies is zero, and the total energy is conserved.

REFERENCES

Adcroft, A., C. Hill, and J. Marshall, 1997: Representation of topography by shaved cells in a height coordinate ocean model. *Mon. Wea. Rev.,* **125,** 2293–2315.

Bleck, R., 1998: Ocean modeling in isopycnic coordinates. *Ocean Modeling and Parameterization,* E. P. Chassignet and J. Vernon, Eds., Kluwer Academic, 423–448.

Bryan, K., 1969: A numerical method for the study of the circulation of the world ocean. *J. Comput. Phys.,* **4,** 347–376.

Cushman-Roisin, B., O. E. Esenkov, and B. J. Mathias, 2000: A particle-in-cell method for the solution of two-layer shallow-water equations. *Int. J. Numer. Meth. Fluids,* **32,** 515–543.

Dukowicz, J. K., and R. D. Smith, 1994: Implicit free-surface method for the Bryan-Cox-Semtner ocean model. *J. Geophys. Res.,* **99,** 7991–8014.

Esenkov, O. E., and B. Cushman-Roisin, 1999: Modeling of two-layer eddies and coastal flows with a particle method. *J. Geophys. Res.,* **104,** 10 959–10 989.

Ezer, T., and G. L. Mellor, 1997: Simulations of the Atlantic Ocean with a free surface sigma coordinate ocean model. *J. Geophys. Res.,* **102,** 15 647–15 657.

Frei, C., 1993: Dynamics of a two-dimensional ribbon of shallow water on an *f*-plane. *Tellus,* **45A,** 44–53.

Griffies, S. M., A. Gnanadesikan, R. C. Pacanowski, V. D. Larichev, J. K. Dukowicz, and R. D. Smith, 1998: Isoneutral diffusion in a *z*-coordinate ocean model. *J. Phys. Oceanogr.,* **28,** 805–830.

——, R. C. Pacanowski, and R. W. Hallberg, 2000: Spurious diapycnal mixing associated with advection in a *z*-coordinate ocean model. *Mon. Wea. Rev.,* **128,** 538–564.

Haidvogel, D. B., H. G. Arango, K. Hedstrom, A. Beckmann, P. Malanotte-Rizzoli, and A. F. Shchepetkin, 2000: Model evaluation experiments in the North Atlantic Basin: Simulations in nonlinear terrain-following coordinates. *Dyn. Atmos. Oceans,* **32,** 239–281.

Haney, R. L., 1991: On the pressure gradient force over steep topography in sigma coordinate ocean models. *J. Phys. Oceanogr.,* **21,** 610–619.

Harlow, F. H., 1964: The particle-in-cell computing method for fluid dynamics. *Methods Comput. Phys.,* **3,** 319–343.

Jensen, T. G., 1996: Artificial retardation of barotropic waves in layered ocean models. *Mon. Wea. Rev.,* **124,** 1272–1283.

——, 2001: Application of the GWR method to the tropical Indian Ocean. *Mon. Wea. Rev.,* **129,** 470–485.

Le Roux, D. Y., C. A. Lin, and A. Staniforth, 2000: A semi-implicit semi-Lagrangian finite-element shallow-water ocean model. *Mon. Wea. Rev.,* **128,** 1384–1401.

Lynch, D. R., J. T. C. Ip, C. E. Namie, and F. E. Werner, 1995: Comprehensive coastal circulation model with application to the Gulf of Maine. *Cont. Shelf Res.,* **16,** 875–906.

Monaghan, J. J., 1992: Smoothed particle hydrodynamics. *Annu. Rev. Astron. Astrophys.,* **30,** 543–574.

——, 1994: Simulating free surface flows with SPH. *J. Comput. Phys.,* **110,** 399–406.

Ochoa, J., J. Sheinbaum, and E. G. Pavia, 1998: Inhomogeneous rodons. *J. Geophys. Res.,* **103,** 24 869–24 880.

Pacanowski, R. C., and A. Gnanadesikan, 1998: Transient response in a *z*-level ocean model that resolves topography with partial cells. *Mon. Wea. Rev.,* **126,** 3248–3270.

Pavia, E. G., 1992: The breakup of frontal filaments. *J. Phys. Oceanogr.,* **22,** 399–403.

——, and B. Cushman-Roisin, 1988: Modeling of oceanic fronts using a particle method. *J. Geophys. Res.,* **93,** 3554–3562.

——, and ——, 1990: Merging of frontal eddies. *J. Phys. Oceanogr.,* **20,** 1886–1906.

——, and M. Lopez, 1994: Long-term evolution of elongated warm eddies. *J. Phys. Oceanogr.,* **24,** 2201–2208.

Phillips, N. A., 1957: A coordinate system having some special advantages for numerical forecasting. *J. Meteor.,* **14,** 184–185.

Roberts, M. J., R. Marsh, A. L. New, and R. A. Wood, 1996: An intercomparison of a Bryan-Cox-type ocean model and an isopycnic ocean model. Part I: The subpolar gyre and high-latitude processes. *J. Phys. Oceanogr.,* **26,** 1495–1527.

Sanson, L. Z., F. Graef, and E. G. Pavia, 1998: Collision of anticyclonic, lens-like eddies with a meridional western boundary. *J. Geophys. Res.,* **103,** 24 881–24 890.

Schär, C., and P. K. Smolarkiewicz, 1996: A synchronous and iterative flux-correction formalism for coupled transport equations. *J. Comput. Phys.,* **128,** 101–120.

Smith, R. D., M. E. Maltrud, F. O. Bryan, and M. W. Hecht, 2000: Numerical simulation of the North Atlantic Ocean at one-tenth degree. *J. Phys. Oceanogr.,* **30,** 1532–1561.

Sun, S., R. Bleck, C. Rooth, J. Dukowicz, E. Chassignet, and P. Killworth, 1999: Inclusion of thermobaricity in isopycnic-coordinate ocean models. *J. Phys. Oceanogr.,* **29,** 2719–2729.